Imaging plant growth in 4D: robust tissue reconstruction and lineaging at cell resolution

Romain Fernandez[1,2,5], Pradeep Das[3,5], Vincent Mirabet[3], Eric Moscardi[1], Jan Traas[3], Jean-Luc Verdeil[4], Grégoire Malandain[2] & Christophe Godin[1]

© 2010 Nature America, Inc. All rights reserved.

Quantitative information on growing organs is required to better understand morphogenesis in both plants and animals. However, detailed analyses of growth patterns at cellular resolution have remained elusive. We developed an approach, multiangle image acquisition, three-dimensional reconstruction and cell segmentation–automated lineage tracking (MARS-ALT), in which we imaged whole organs from multiple angles, computationally merged and segmented these images to provide accurate cell identification in three dimensions and automatically tracked cell lineages through multiple rounds of cell division during development. Using these methods, we quantitatively analyzed *Arabidopsis thaliana* flower development at cell resolution, which revealed differential growth patterns of key regions during early stages of floral morphogenesis. Lastly, using rice roots, we demonstrated that this approach is both generic and scalable.

The control of morphogenesis during plant and animal development is a major question in developmental biology. Although several studies have provided profound insight into the molecular regulatory networks that act during development, the effects of such networks on shape transformations are often only described qualitatively. Indeed, describing shape and shape change as a geometrical output of gene activity requires the quantification of growth patterns with cellular resolution. Obtaining accurate geometric information about cell positions and shapes will be essential to develop quantitative growth models[1–6] and to accurately test their predictions. Although several recent methods, mostly based on nuclear tracking in animal cell populations[7–10], have addressed cell positioning and tracking, they cannot provide information on three-dimensional (3D) cell geometry.

We are interested in characterizing and quantifying growth in plant meristems, which are small groups of pluripotent cells that give rise to all organs in both the shoot and the root. Three types of meristems can be identified: the root apical meristem, the shoot apical meristem and the floral meristem. Meristem size may vary from a few cells to several thousand cells, depending on the species and the meristem type. In *Arabidopsis thaliana*, an initiating floral meristem measures 20–35 μm along each axis and contains 30–50 cells, each ~150–250 μm^3. With divisions every 19–24 h on average[11], the flower quickly grows into an object measuring 80–100 μm along each axis and containing several hundred cells, even before the onset of differentiation and organ formation. Rice root meristems, in contrast, may contain many thousands of cells[12]. Plant cells are typically separated from each other by cell walls and cell membranes of less than 0.5 μm in thickness, whose correct identification is essential to accurately determine cell shapes.

Different methods have been used to image and reconstruct tissues at cellular resolution[7–10,13–15]. Confocal laser-scanning microscopy has been used to image fixed roots and to semiautomatically identify individual cells[16]. In living plant tissues, most protocols have been restricted to surface reconstructions[17–19]. Confocal microscopy has the advantage of providing access to the inner parts of the tissue, but the fluorescence signal fades in the inner parts of thick tissue, making it difficult to identify cell walls in the deeper layers. Additionally, cell walls perpendicular to the focal axis of the microscope are very often not seen. These drawbacks severely limit the use of automatic processing to extract additional information from confocal images. Here we present a method to generate 3D digitized tissues at cell resolution and to automatically track cell lineage during growth. To create a digitized tissue that can be used to quantitatively analyze growth in four dimensions, we developed an experimental pipeline comprising two key steps: multiangle image acquisition, 3D reconstruction and cell segmentation (MARS) and automated lineage tracking (ALT). We applied this pipeline to analyze the developmental dynamics of young floral meristems over 70 h.

RESULTS

Multi-angle, real-time imaging via confocal microscopy

To overcome limitations owing to either tissue thickness or microscope resolution anisotropy (**Supplementary Fig. 1**), we

[1]Equipe-projet Virtual Plants, Institut National de la Recherche en Informatique et en Automatique, Sophia Antipolis, France and Unité Mixte de Recherche Développement et Adaptation des Plantes, Montpellier, France. [2]Equipe-projet Asclepios, Institut National de la Recherche en Informatique et en Automatique, Sophia Antipolis, France. [3]Laboratoire Reproduction et Développement des Plantes, Ecole Normale Supérieure de Lyon et Institut National de la Recherche Agronomique, Lyon, France. [4]Centre de Coopération Internationale en Recherche Agronomique pour le Développement et Unité Mixte de Recherche Développement et Adaptation des Plantes, Montpellier, France. [5]These authors contributed equally to this work. Correspondence should be addressed to C.G. (christophe.godin@inria.fr).

RECEIVED 19 OCTOBER 2009; ACCEPTED 14 MAY 2010; PUBLISHED ONLINE 13 JUNE 2010; DOI:10.1038/NMETH.1472

devised MARS based on the idea of visualizing a single sample from multiple angles (**Fig. 1a**). We stained shoot apical meristems bearing only flower buds between stages 1 and 3 with the vital dye FM4-64 and imaged them under a confocal laser-scanning microscope (Online Methods). First we imaged the flower from the top ('top-view stack'), and then we manually tilted it by 30–40° and reimaged it ('tilt-view stack'). We repeated this process such that we imaged every flower from at least three different angles (**Fig. 1b–d**). We avoided rotation angles greater than 50° to maintain sufficient common context between each image.

3D reconstruction and segmentation of volumetric images

We computed 3D cell-segmented images from multiangle scans in two steps. First, we fused the images acquired under different orientations to enhance the quality of the cell outlines (**Supplementary Note 1**), which required co-registering every image stack with a reference stack. We used a hierarchical strategy wherein, for convenience, we chose the top-view stack as the reference stack and in an incremental procedure registered the other (floating) tilt-view stacks onto this reference. Based on at least four landmarks that we manually identified in both the reference and the floating stacks (**Fig. 1b–d** and **Supplementary Fig. 2**) using surface reconstructions[19], we computed an initial rigid transformation (which consisted of rotation and translation; **Fig. 1e**). This first step usually yielded only an approximate matching (**Fig. 1f**), possibly because of local shape changes resulting from plant growth or from changes in the mechanical or physiological properties of the cells. Then, a more robust, rigid transformation was automatically computed using all available image information[20], followed by a refined nonlinear transformation computed using a block-based pyramidal algorithm[21] (**Fig. 1g,h**). This process substantially restored membrane-to-cytoplasm contrast in the entire 3D structure and also typically provided a much more homogeneous contrast distribution in the tissue (**Fig. 1i,j** and **Supplementary Fig. 3**).

Second, we segmented the resultant 3D images using a 3D watershed algorithm[22] to identify the cells as individual 3D objects (**Fig. 1k–m** and **Supplementary Note 2**). Such an algorithm is well suited for processing our images, in which the objects to segment were dark areas (cell interiors) surrounded by bright and thin boundaries (cell walls). To initialize the procedure, every cell must have a unique marker. We defined these markers as the main local minima (computed using the *h*-min operator[22]) of the noise-filtered image.

We next assessed whether MARS was generic and scalable by applying it to rice roots, which are large (200–450 μm) and have a complex cellular organization (with about 30 cell layers)[23]. We observed the root meristem under four azimuthal angles spaced approximately 90 degrees from one another. The cell recognition was of better quality in the four-fused-view reconstructions than in the one-view reconstructions: the algorithm could segment 16,400 cells in the rice root tip for the four fused views and for one view with an estimated cell recognition rate of 88% and 61% in the root center, and of 93% and 87% in the cortical region, respectively (Online Methods, **Supplementary Figs. 4** and **5** and **Supplementary Note 3**).

Automatic lineage tracking during growth

To identify cell lineages during floral growth, we developed a second software pipeline called ALT (**Fig. 2a**). First, we used MARS to track the growth of young flower meristems (primordia) by imaging them from multiple angles every 24 h for up to 4 d and generating 3D cell-segmented images at each time point (**Fig. 2b–i**

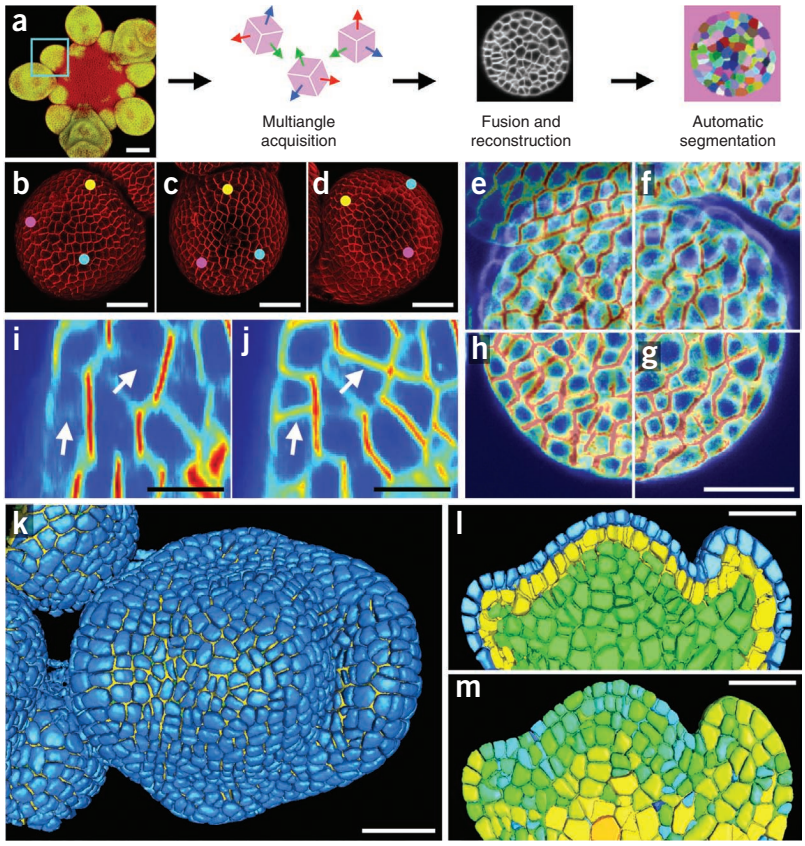

Figure 1 | MARS. (**a**) Pipeline for segmented 3D tissue reconstructions. From an image of inflorescence expressing a flower-specific *GFP* marker (*pLEAFY::ER-GFP*), one flower (blue box) is chosen for further study (left). For each flower, image stacks are acquired from multiple angles and computationally fused into a single 3D reconstruction, which is then automatically segmented. (**b–d**) Example confocal images of a flower acquired from three angles. After image acquisition, three to eight common landmark vertices (colored dots) are identified in each image stack. (**e–h**) These image stacks are registered using a hierarchical process with increasing precision and then fused as follows: superposition of the raw images from two different views (**e**), a manual, rigid registration (**f**), an automatic, linear registration (**g**) and a dense, nonlinear registration (**h**). (**i,j**) Images showing details of single-angle (**i**) and fused multiangle (**j**) acquisitions. Arrows highlight signal for cell outlines and interiors that is low or absent in single-angle images. (**k–m**) After automatic segmentation, tissue was visualized with a full organ reconstruction (**k**) or with virtual sections using color codes for cell layer (**l**) or cell volume (**m**). Scale bars, 50 μm (**a**), 25 μm (**b–h,k–m**) and ~10 μm (**i,j**).

© 2010 Nature America, Inc. All rights reserved.

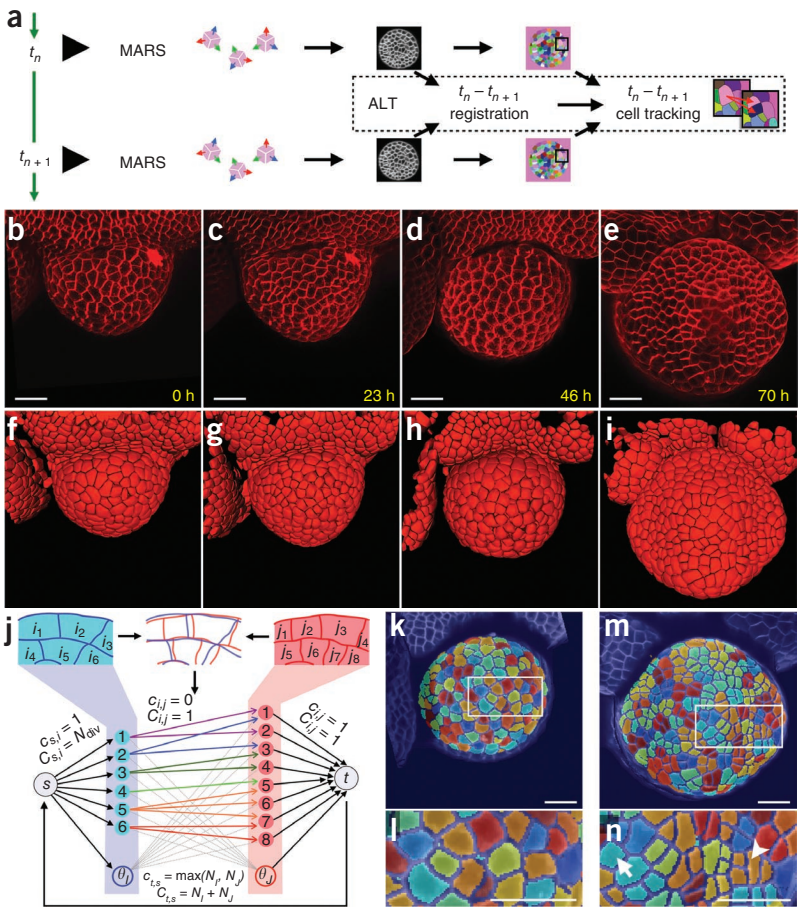

Figure 2 | ALT. (**a**) ALT pipeline. Reconstructed and segmented data from serial time points (t_n and t_{n+1}) are compared to automatically determine cell lineages. (**b–e**) Confocal image surface projections of the top view of a wild-type flower collected at the indicated times. (**f–i**) Segmented 3D reconstructions of each time point (corresponding to images in **b–e**, respectively), with many cells belonging to the shoot apex and to neighboring flowers manually discarded. (**j**) ALT is modeled as a problem of flow in which plausible lineage correspondences are expressed in a valued graph. Edges connect parent cells of the source image (i_{1-6}) to candidate daughter cells of the target image (j_{1-8}). θ_I, θ_J, s and t are additional nodes representing, respectively, void source cell, void target cell and source and target nodes emitting and collecting the flow. Each edge may carry units of flow that are bounded by the edge minimal and maximal capacities, $c_{i,j}$ and $C_{i,j}$, respectively, and is associated with a cost per unit flow. N_I and N_J, the number of source and target cells, respectively; N_{div}, hypothesized maximum number of daughters that can be associated with a given parent. (**k–n**) Application of the ALT algorithm to floral growth: cells at an earlier time point (**k**,**l**) and corresponding daughter cells (**m**,**n**) were colored to show lineages. Detailed views (**l**,**n**) show cells that have undergone up to two rounds of cell division (arrowhead). Also visible is a tracking error (cell marked with an arrow should be red). Scale bars, 10 μm.

© 2010 Nature America, Inc. All rights reserved.

and **Supplementary Fig. 6**). Next, we manually identified an initial set of surface (L1 layer) cell lineages for every pair of consecutive segmented images from sequential time points (**Supplementary Note 4**). We used these 'known' reference lineages to initialize the set of high-confidence lineages of the ALT pipeline. ALT begins by estimating a rigid transformation between two images by minimizing the total square distance between parent cells and their descendants in high-confidence lineages. It then estimates new high-confidence cell lineages iteratively by performing the following steps until no candidate cell lineages remain (**Supplementary Note 4**).

In the first step, ALT computes a deformation field based on the high-confidence lineages. The residual positioning error is used to define a nonlinear transformation of the image voxels as a dense vector field (a vector per voxel). For this, each high-confidence lineage is transformed into one vector that links the center of mass of the parent cell to the center of mass of all its descendants, and the dense vector field is computed by interpolating between these vectors.

In the second step, the deformation field is refined. The initial nonlinear transformation is refined by an automated nonlinear registration algorithm that matches the voxel intensities of the two images. This defines a more precise nonlinear registration that makes it possible to overlap the two images and compare their segmentations.

In the third step, ALT builds lineage hypotheses and solves the lineage problem. Pairwise registration of sequential images permits candidate daughter cells for each parent cell to be hypothesized, based on their spatial proximity in a common image frame. ALT formalizes the lineage problem as the search for a mapping between cells in sequential images that globally minimizes the total distances between the mapped cells. To solve this problem, ALT treats it as an optimal flow problem (**Fig. 2j**, **Supplementary Note 4** and Online Methods).

In the final step, ALT updates the set of high-confidence lineages. ALT automatically scans the list of lineages between two images to identify those lineages that comply with additional criteria (**Supplementary Note 4**) by applying plausibility tests based on geometric and topological rules that are not used to guide the algorithm. If a cell lineage passes the test, it is then added to the list of high-confidence lineages.

We used the ALT algorithm to identify lineages during flower growth over 70 h (**Fig. 2k–n**). ALT provided 84–100% accurate cell lineage information, depending on the extent of growth (**Table 1** and Online Methods).

Validation of the MARS-ALT pipeline

We assessed the quality of the segmentation algorithm by an exhaustive visual examination of the results obtained from the automatic segmentations of *Arabidopsis* floral meristems. We examined eight MARS-analyzed floral meristems cell by cell using MARS exploratory tools (**Supplementary Note 5**). This included one flower ('flower A') imaged at an optimal resolution (varying from 576 × 576 to 680 × 680 pixels) at four time points separated by about 24 h each, and two flowers ('flower 2' and 'flower 3') imaged at a higher resolution (1,024 × 1,024 pixels)

Table 1 | Results of the MARS-ALT pipeline applied to flower development

	T_0 (0 h)	T_1 (23 h)	T_2 (46 h)	T_3 (70 h)
Segmentation (MARS)				
Total number of cells imaged and segmented	716	798	706	1,236
Mean cell volume (μm^3)	212	189	250	299
Number of epidermal (L1 layer) cells	344	405	253	379
Number of subepidermal (L2 layer) cells	254	276	251	351
Percentage of correct MARS-segmented cells	97.8	96.2	98.6	98.1
Lineage tracking (ALT)[a]				
Total number of cells tracked by ALT	357	444	582	1236
Increase in total volume of cells tracked during T_0–T_3[b]	NA	1.04-fold	2.26-fold	2.50-fold
S.d. of parent cell volume increase in a T_0–T_3 transition	NA	0.29	0.94	1.38
Reference lineages provided for ALT initialization	4	26	33	NA
Cells with one daughter at the next time point (no division)	252	194	141	NA
Cells with two daughters (1 division)	94	154	240	NA
Cells with three daughters (2 divisions)	1	16	109	NA
Cells with four daughters (3 divisions)	0	4	51	NA
Cell lineages identified manually for ALT evaluation[c]	98	129	184	NA
Percentage of correctly detected mother-to-daughter lineages[d]	100	89	84	NA
Percentage of correctly detected daughter-to-mother lineages[e]	NA	100	94	94

All data presented are from the 'flower-A' time-course experiment (**Fig. 2a**). NA, not applicable.
[a]For clarity, only the ancestors of cells present at T_3 were retained for analysis. [b]At T_0, the total volume of the 357 T_0–T_3-tracked cells was 77.5 × 10^3 μm^3. The fold-increase values in the table are based on the automatically tracked cells. As a consequence, they may be slightly affected by lineage errors. [c]A manual lineage identification was performed to determine the ancestors of all epidermal and subepidermal cells in the upper part of the flower bud (up to and including the sepals) at T_3. [d]This is the most strict definition of a lineage wherein, for a given parent cell, ALT provides the identical set of daughters that had been identified manually. [e]In this definition of a correct lineage, for any given daughter cell, ALT provides the same parent cell that had been identified manually.

© 2010 Nature America, Inc. All rights reserved.

at two time points each. We created a reference segmentation for each of these multiangle images by manually correcting an automatic segmentation. To assess the performances of different segmentation algorithms or the effect of varying their parameters, we compared, for a given image, the automatic segmentation produced by these algorithms to the reference segmentation of this image. As two segmentations, each containing hundreds of cells in three dimensions, cannot be manually compared routinely, we designed a special algorithm to automate this comparison process (**Supplementary Note 6**). We considered cells correctly identified if they could be associated one-to-one with a manually corrected cell by the validation mapping algorithm.

Merging increasing numbers of view stacks made it possible to substantially increase the percentage of correctly segmented cells. Thus, when a view stack alone was processed, 91.2% of cells were correctly identified (**Fig. 3a**). With the addition of one and two tilt-view stacks, identification improved to 95.7% and 98.5%, respectively. Additional analysis revealed that in one- and two-angle segmentations, only about 60.9% and 81.5% of cells, respectively, had the correct volume relative to the reference segmentations (**Fig. 3b**). Here we considered cells correctly identified if, in addition to the above criterion, the volume of the mapped cells differed by a maximum of 10%. Image resolution had little effect on the efficiency of the algorithm, so that the results obtained for images acquired at optimal resolution or with oversampling differed by only about 2% (data not shown). We then analyzed how the segmentation errors were distributed in the data for floral meristem. As expected, in one-angle segmentations, the percentage of correctly segmented cells decreased steadily with the depth of the tissue (**Fig. 3c**). The fusion of one or two additional view stacks made it possible to substantially improve segmentation quality (**Fig. 3c**) such that at depths greater than 40 μm, up to 7% more cells were correctly identified.

We analyzed how the cell wall signal depended on both its orientation with respect to the focal axis of the microscope and on its depth in the tissue. Cell walls with different orientations have different projected silhouettes in the focal plane. We defined the ratio between the silhouette area of a cell wall projected in the focal plane and the total actual area of the wall as the silhouette to total area ratio (STAR), which has values between 0 and 1. Values close to 1 are reported for cell walls parallel to the focal plane, and values close to 0 are reported for cell walls perpendicular to it. The use of multiangle acquisitions enhanced the contrast for the different categories of cell-wall orientations (**Fig. 3d**), with particular improvement in regions with high STAR (that is, walls nearly parallel to the focal plane) in the reference image stack. Distribution of cell-wall orientations was not homogeneous in the tissue (**Fig. 3e**). At the meristem surface, cell walls had a horizontal bias (STAR > 0.5), consistent with our observation that segmentation quality for surface cells was lower in single-angle segmentations (**Fig. 3c**). The use of multiple angles efficiently corrected this effect of the wall orientation distribution.

To assess the quality of the automatic cell-lineage tracking procedure, we used the four time points (T_0 to T_3) from the flower-A data (**Fig. 2b–i**) and validated the MARS-processed segmentations with the automated procedure described above (**Table 1**). We then manually identified a large number, k_i, of reference lineages between parent cells (at T_{i-1}) and daughter cells (T_i) for each time transition (i = 1, 2 or 3, k_1 = 98, k_2 = 129 and k_3 = 184 lineages) in superficial as well as internal cells. We compared the results of the ALT pipeline to these manually identified reference lineages (**Table 1**). About half the cells at time T_0 yielded daughter cells at time T_3, which corresponded to an average of 3.5 daughter cells at T_3 per parent cell at T_0, for a 4.8-fold volume increase of the corresponding growing region. Our data showed a burst of growth between T_2 and T_3, during which both the volume and the cell division rate increased. When the change in volume was small (T_0 to T_1), ALT correctly identified all of the reference lineages. The performance was slightly worse (89% of cell lineages identified) with a twofold increase in volume. With even bigger

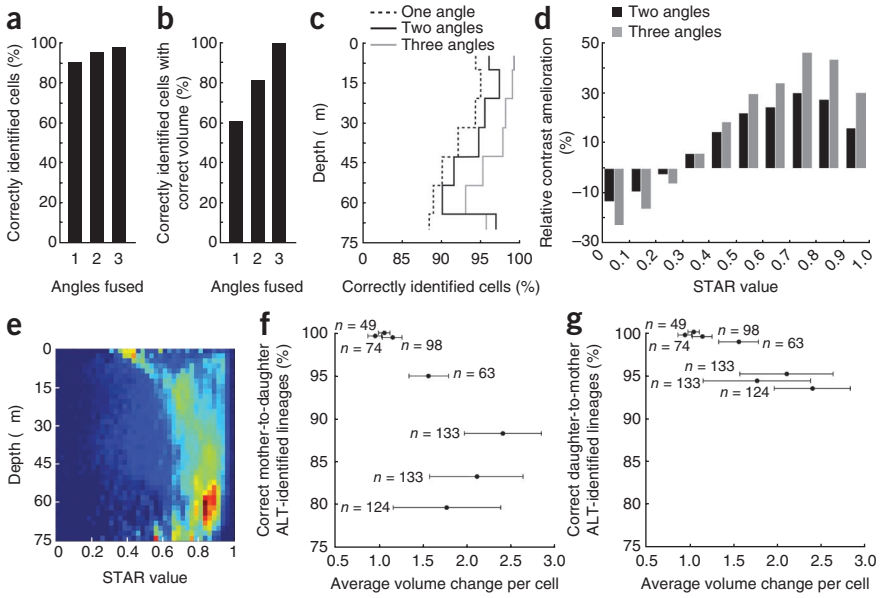

Figure 3 | Validation of MARS-ALT results. (**a**–**d**) Comparisons of eight individual flowers (representing 6,038 cells) that were segmented using reconstructions from one, two or three image stacks. Plotted are data for correctly identified cells (**a**) and correctly identified cells with correct volume (**b**) relative to the manually curated three-angle segmentation. Percentage of correctly segmented cells as a function of depth in the tissue in reconstructions compared to the manual 3-angle segmentation was plotted (**c**; depth was measured along the focal axis of the reference image relative to the meristem surface). Relative amelioration of contrast (**d**) between cell membrane signal and cell interiors (that is, the quality of cell outlines) for various cell membrane orientations relative to one-angle reconstructions was graphed. STAR is a measure of cell-membrane orientation. (**e**) Heat map of cell membrane orientation distribution as a function of depth in the flower. Red color, high values of the distribution, and blue, low values. (**f**,**g**) ALT results from time-course experiments covering different developmental stages from different flowers, showing percentage of mother cells with fully correct daughter cells (**f**) or percentage of daughter cells with correct mother cells (**g**) for average volume change per cell. Horizontal lines show s.d. (n = 49–184 lineages, depending on the point in the diagram). Points clustered at 100% were manually separated for clarity.

increases of volume (2.5-fold between T_2 and T_3), only 84% of the cell lineages were perfectly identified. But this corresponded to an incorrect detection of a parent cell for only 6% of daughter cells. By extrapolation to the entire dataset, ALT correctly detected the parent cell for 1,162 of the 1,236 cells at T_3. We observed similar trends in other time-course experiments (**Fig. 3f**,**g**).

The ALT algorithm identifies not only the cellular lineages but also the precise geometrical deformations that occur during growth. Based on this four-dimensional reconstruction, it is possible to estimate the intermediate 3D images by interpolation between serial time steps. This virtual 3D representation of continuous growth at cellular resolution is a powerful way to observe organ-growth dynamics (**Supplementary Note 7** and **Supplementary Videos 1** and **2**).

Analysis of early floral growth at cellular resolution

The *Arabidopsis* flower initiates on the flanks of the shoot apical meristem as a stage-1 bud. During stage 2, the bud becomes separated from the shoot apical meristem and goes through a long growth phase. The first organs form at stage 3, when the flower bud comprises four sepal primordia surrounding a dome of meristematic tissue in the center, which gives rise to all other floral organs. We used MARS-ALT to analyze cell lineage trajectories and cell morphometrics of this entire zone in two independent time-course experiments (**Fig. 4a**).

First, we used the digital reconstructions of the last time points in both time courses, selected all the cells of the sepals and the floral dome (the 'floral organ zone') and used ALT to identify these cells' ancestors at the earliest time points in the two experiments. We then mapped the locations of those ancestors in the flower and observed that at mid–stage 2, these cells were located not at the vertical summit of the flower, but abaxially, in the region most distal to the shoot apical meristem (**Fig. 4b**,**c**). This suggests that as the flower develops, it undergoes unequal growth along the medial (proximo-distal) axis that pushes the abaxial cells toward the summit (**Fig. 4d**). We next investigated whether such an unequal tissue growth was linked to particular cellular characteristics, such as cell size. We analyzed cell volumes during floral growth (**Fig. 4e** and **Supplementary Fig. 7**). We observed that at stage 3 in both time-course experiments, the floral organ zone cells had significantly similar mean volumes (195 ± 88 μm^3 for flower A (n = 674 cells); 195 ± 102 μm^3 for flower B (n = 611 cells); P = 0.9833 in a Welch two-sample t-test). However, during the transition from stage 2 to 3, many cells (12%, 70 h of flower A time course) grew to volumes of over 500 μm^3 (**Fig. 4e**). We observed that all of these cells were located below the floral organ zone and likely belonged either to the emerging vascular strands or to the elongating pedicel (**Fig. 4f**). Whereas the smallest cells in this group (500–600 μm^3) were distributed uniformly around the base of the flower (**Fig. 4g**), the largest cells (1,000–2,200 μm^3) were located primarily along the abaxial side of the flower (**Fig. 4h**). Thus, in contrast to the majority of cells, these cells had not divided in this 24 h period. These data suggest that changes in cell division rules are an important part of floral growth and specification and that these rules may be altered locally to control morphogenesis.

To explore cellular growth and dynamics in the floral organ zone, we examined the stem cells and the stem cell organizing center, which are crucial for proper flower development. We localized the putative stem cells and organizing center over time using a stem cell–specific reporter line. Consistent with our findings for the floral organ zone, the putative stem cells and organizing center ancestors were also located in an abaxial region at early stages (**Supplementary Fig. 8**). It has long been suggested that organizing center cells are large and slow dividing[24], but it has never been possible to properly examine their morphologies or dynamics in four dimensions. We found that at early mid–stage 2, the uppermost (L3 layer) putative organizing center cell had an exceptionally large volume (402 μm^3 in flower-A data) that was almost twice the mean volume of all floral cells (212 μm^3; **Table 1**). Descendants of this cell formed a tight cluster at stage 3,

© 2010 Nature America, Inc. All rights reserved.

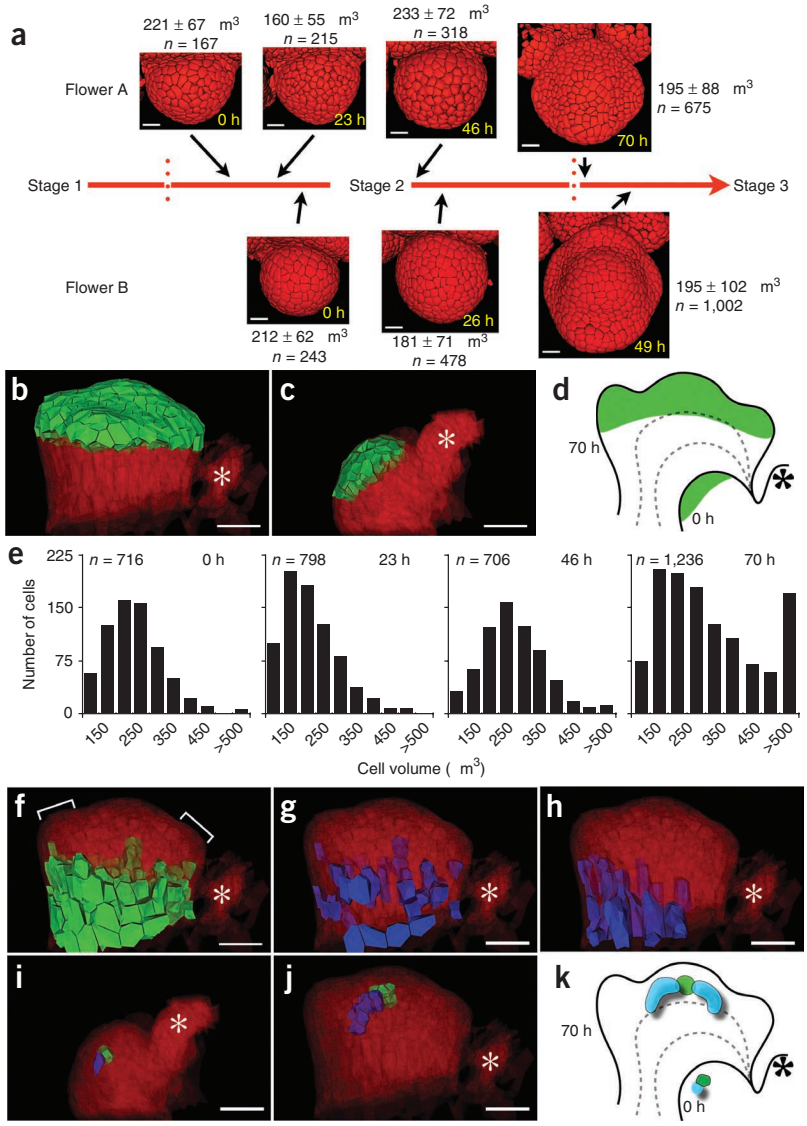

Figure 4 | Application of MARS-ALT to flower development. (**a**) Reconstructions from two MARS-ALT time-course experiments (flower A and flower B) tracking wild-type floral growth. For comparison, stages 1–3 are positioned on a common timeline. Times of image acquisition (which are unrelated between the two experiments) and mean volumes (±s.d.) of cells in the floral organ zone are indicated. (**b**–**k**) Image renderings and schematics are side views of reconstructed flower A at early mid–stage 2 (**c**,**i**) or early stage 3 (**b**,**f**–**h**,**j**). The flower and a part of the shoot apical meristem (asterisk) are shown in red, with cells of interest in green or blue. Side view at 70 h with all floral organ zone cells selected (**b**) and at 0 h showing the ancestors of the cells in **b** (**c**). The schematic in **d** shows growth along the proximo-distal axis with the first and last time points drawn as solid lines and intermediate stages represented as dashed lines. Frequency distributions (**e**) of cell volumes from flower A during growth. Rendering at 70 h with 143 large cells marked (**f**; green). The smallest (**g**; 500–600 μm^3) and the largest (**h**; >1,000 μm^3) of the marked cells in **f** are shown. Rendering in **i** shows a single stem cell organizing center cell (green) at 0 h and one immediate neighbor (blue). Daughter cells of both cells in **i** at 70 h are shown in **j**. (**k**) Schematic contrasting growth of the organizing center cell and that of its neighbor is shown in **k** (as in **d**). Scale bars, 10 µm (**a**), and ~25 µm (**b**,**c**,**f**–**j**).

whereas descendants of its immediate neighbors tended to form cell files that extended away from the organizing center cluster (**Fig. 4i–k**), reflecting local anisotropic cell growth that presumably contributes to the emergence of floral shape at stage 3.

By enabling examination of specific cells or groups of cells, MARS-ALT allowed us to analyze floral growth emergence. A powerful extension of this analysis will be to combine such studies with cellular identities (for instance, using cell-fate reporters) to clarify the temporal link between local growth properties and differentiation events.

DISCUSSION

Our pipeline has some key advantages over existing methods. In contrast to published *ad hoc* methods of fusing multiple images[25], MARS requires neither dedicated hardware nor precise external landmarks to guide the fusion. It works at cellular resolution, can efficiently segment internal cells deep in living tissues, can efficiently segment very large numbers of cells and can be applied to images with different markers (**Supplementary Fig. 9**). In contrast to methods that track nuclei in growing tissues at very small time intervals (typically one image per minute)[7], the combination of MARS and ALT allowed us to describe growth deformations in the entire cell and over long developmental time periods. Thus, we can begin to describe floral morphogenesis in terms of the morphological changes in component cells. As our lineage tracking algorithm relies on a global optimization procedure, it is very robust to local segmentation or tracking errors. Furthermore, as we designed the pipeline with no plant-specific dependencies, it should be applicable to other biological systems, with adaptation to address cell movement and/or cell death in animal tissues. Our algorithm already accommodates the loss of cells (for example, those that leave the field of view), and should thus be able to 'accept' cell death. The fact that the topology should not change in vegetal cells during growth is only used in ALT to select the most probable cell lineages (**Supplementary Note 4**). This test may be removed or weakened for use with animal tissues. It may be possible to address the issue of cell movement just by generating sufficiently clustered time point data.

One limitation of our algorithms is that the error rate for lineage tracking tends to increase with increasing extent of change (deformation and/or cell divisions) that the tissue undergoes during growth (**Fig. 3f,g** and **Supplementary Fig. 7**). Thus, during periods of rapid growth in a tissue, shortening the time interval between two acquisitions (and thus limiting the extent of change) may be required to obtain highly accurate ALT results. For 90% accurate daughter-to-mother cell lineage recognition, time intervals will have to be adjusted to maintain the s.d. of

© 2010 Nature America, Inc. All rights reserved.

volume expansion (which reflects nonhomogeneous tissue deformation) below 0.8 (**Supplementary Fig. 7**). A second limitation is that because our current floral analyses have been focused on the early stages, our experiments have not used time windows of more than a few days. It is possible that the biological protocols may require modification for much longer time course experiments. It will be necessary to determine the optimal time window to accurately observe certain developmental phase changes, as floral growth is not a temporally linear process. Furthermore, because the vital stain appears to have some toxic effects upon prolonged exposure, other fluorescent membrane markers (such as GFP fusions) may be needed. Finally, in the long term, scaling up the pipeline to improve throughput may present potential problems from an algorithmic point of view, such as in automatically identifying input reference points for MARS and reference lineages for ALT. These are challenging, highly combinatorial operations that will require additional development and testing to reach complete (or near-complete) automation.

Our work has many potential applications. First, MARS-ALT provides the opportunity for developmental biologists to quantitatively examine organ growth and track growth rate, anisotropy and growth direction in both surface and internal cells. Incorporation of reporter expression could enable linking quantitative growth analyses to gene activity and cellular identity. Second, our digitized floral growth template provides an opportunity to use 3D computational modeling to quantitatively test biological hypotheses. Third, we can now address a longstanding question on the precise nature of cell division rules in growing tissues and organs. Finally, our approaches may be used to examine and model organ growth in mutants with the aim of quantifying affected cellular behaviors and generating hypotheses on mechanisms that control them. This will serve to link the activities of specific genes to their morphogenetic outputs at cellular resolution.

METHODS

Methods and any associated references are available in the online version of the paper at http://www.nature.com/naturemethods/.

Note: Supplementary information is available on the Nature Methods website.

ACKNOWLEDGMENTS

We thank A. Berger for help with establishing plant growth and imaging protocols; A. Lacroix for help with plant growth; and C. Lionnet for help with imaging. This work was funded by grants from the Centre de Coopération Internationale en Recherche Agronomique pour le Développement (to J.-L.V.), the Region Languedoc-Roussillon (to R.F.) and from the Institut National de la Recherche en Informatique et en Automatique (to C.G.). P.D. was funded by a European Union Marie Curie Incoming International Fellowship grant (IIF-022002). The work of J.T. and C.G. was also funded by grants from the Agence Nationale de Recherche (Virtual Carpel, GeneShape and Flower model) and the European Union (Morphex).

AUTHOR CONTRIBUTIONS

P.D., J.T., J.-L.V., G.M. and C.G. conceived the experiments; P.D. carried out the *Arabidopsis* experiments; J.-L.V. carried out the rice experiments; R.F., G.M. and C.G. conceived the software pipeline; R.F. wrote the software; R.F., E.M. and V.M. carried out the software experiments; E.M. and R.F. wrote the MARS-ALT documentation; P.D. and V.M. analyzed the output; P.D., G.M. and C.G. wrote the paper with input from the other authors.

COMPETING FINANCIAL INTERESTS

The authors declare no competing financial interests.

Published online at http://www.nature.com/naturemethods/.
Reprints and permissions information is available online at http://npg.nature.com/reprintsandpermissions/.

1. Coen, E., Rolland-Lagan, A.G., Matthews, M., Bangham, J.A. & Prusinkiewicz, P. The genetics of geometry. *Proc. Natl. Acad. Sci. USA* **101**, 4728–4735 (2004).
2. Smith, R. *et al.* A plausible model of phyllotaxis. *Proc. Natl. Acad. Sci. USA* **103**, 1301–1306 (2006).
3. Jonsson, H., Heisler, M.G., Shapiro, B.E., Meyerowitz, E.M. & Mjolsness, E. An auxin-driven polarized transport model for phyllotaxis. *Proc. Natl. Acad. Sci. USA* **103**, 1633–1638 (2006).
4. Jonsson, H. *et al.* Modeling the organization of the WUSCHEL expression domain in the shoot apical meristem. *Bioinformatics* **21** (Suppl. 1), i232–i240 (2005).
5. Barbier de Reuille, P. *et al.* Computer simulations reveal properties of the cell–cell signaling network at the shoot apex in *Arabidopsis*. *Proc. Natl. Acad. Sci. USA* **103**, 1627–1632 (2006).
6. Hamant, O. *et al.* Developmental patterning by mechanical signals in *Arabidopsis*. *Science* **322**, 1650–1655 (2008).
7. Bao, Z. *et al.* Automated cell lineage tracing in *Caenorhabditis elegans*. *Proc. Natl. Acad. Sci. USA* **103**, 2707–2712 (2006).
8. Verveer, P.J. *et al.* High-resolution three-dimensional imaging of large specimens with light sheet-based microscopy. *Nat. Methods* **4**, 311–313 (2007).
9. Jaqaman, K. *et al.* Robust single-particle tracking in live-cell time-lapse sequences. *Nat. Methods* **5**, 695–702 (2008).
10. Murray, J.I. *et al.* Automated analysis of embryonic gene expression with cellular resolution in *C. elegans*. *Nat. Methods* **5**, 703–709 (2008).
11. Reddy, G.V., Heisler, M.G., Ehrhardt, D.W. & Meyerowitz, E.M. Real-time lineage analysis reveals oriented cell divisions associated with morphogenesis at the shoot apex of *Arabidopsis thaliana*. *Development* **131**, 4225–4237 (2004).
12. Verdeil, J., Alemanno, L., Niemenak, N. & Tranbarger, T. Pluripotent versus totipotent plant stem cells: dependence versus autonomy? *Trends Plant Sci.* **12**, 245–252 (2007).
13. Boot, M.J. *et al.* *In vitro* whole-organ imaging: 4D quantification of growing mouse limb buds. *Nat. Methods* **5**, 609–612 (2008).
14. Huisken, J., Swoger, J., Del Bene, F., Wittbrodt, J. & Stelzer, E.H. Optical sectioning deep inside live embryos by selective plane illumination microscopy. *Science* **305**, 1007–1009 (2004).
15. Long, F., Peng, H., Liu, X., Kim, S.K. & Myers, E. A 3D digital atlas of *C. elegans* and its application to single-cell analyses. *Nat. Methods* **6**, 667–672 (2009).
16. Moreno, N., Bougourd, S., Haseloff, J. & Feijo, J. in *Handbook of Biological Confocal Microscopy*, 3rd edn. (ed., J.B. Pawley) (Springer Science+Business Media, New York, 2006).
17. Kwiatkowska, D. Surface growth at the reproductive shoot apex of *Arabidopsis* thaliana pin-formed 1 and wild type. *J. Exp. Bot.* **55**, 1021–1032 (2004).
18. Grandjean, O. *et al.* *In vivo* analysis of cell division, cell growth, and differentiation at the shoot apical meristem in *Arabidopsis*. *Plant Cell* **16**, 74–87 (2004).
19. Barbier de Reuille, P., Bohn-Courseau, I., Godin, C. & Traas, J. A protocol to analyse cellular dynamics during plant development. *Plant J.* **44**, 1045–1053 (2005).
20. Ourselin, S., Roche, A., Prima, S. & Ayache, N. Block matching: a general framework to improve robustness of rigid registration of medical images. in *Third International Conference on Medical Robotics, Imaging And Computer Assisted Surgery* (eds., DiGioia, A.M. and Delp, S.) 557–566 (Springer, 2000).
21. Commowick, O. & Malandain, G. From statistical atlases to personalized models. in *Proceedings of the SA2PM Workshop* (2006).
22. Soille, P. *Morphological Image Analysis: Principles and Applications* 89–125 (Springer-Verlag, Berlin, 1999).
23. Rebouillat, J. *et al.* Molecular genetics of rice root development. *Rice* **2**, 15–34 (2009).
24. Steeves, S. & Sussex, I.M. *Patterns in Plant Development* (Cambridge University Press, 1989).
25. Preibisch, S., Saalfeld, S., Rohlfing, T. & Tomancak, P. Bead-based mosaicing of single plane illumination microscopy images using geometric local descriptor matching. *Proc. SPIE* **72592S**, 1–10 (2009).

© 2010 Nature America, Inc. All rights reserved.

ONLINE METHODS

Plant growth and imaging. *Arabidopsis* plants were grown as described previously[26]. Approximately 2 cm of the upper part of the plant, including the shoot apical meristem and the flowers, were placed in growth medium. All flower buds older than stage 3 were then dissected away to facilitate observations of early stage flowers. During time course experiments, plants were maintained in growth chambers between acquisitions, and, if necessary, older flower buds were removed. In general, only one flower from any given inflorescence meristem was tracked over time, to limit damage from handling. Just before imaging, inflorescences were treated with about 2 µl (of a 330 µg ml^{-1} stock) of the water-soluble lipophilic dye FM 4-64 (Invitrogen), which labels cell membranes. The treated inflorescences were then immersed in water and observed on a Zeiss LSM 510 confocal microscope with a 63× water immersion achroplan lens with a 2 mm working distance. Images were acquired at a resolution of 0.2 µm along *x* and *y* axes and 1 µm along the *z* axis. The meristems were manually rotated between angle scans, a process that took 2–5 min, which equates to a total acquisition time of 45–60 min per flower at each time point. Each set of multiangle scans took 45–60 min to acquire. In experiments in which the flowers were imaged multiple times, the inflorescence meristems were returned to a culture chamber after each observation and relabeled with FM4-64 before subsequent imaging.

All flowers presented here were either in the Columbia (Col) or the Wassilewskija (Ws) ecotypes. 'Flower 3' and 'flower 2' were observed at high resolution (1,024 × 1,024 pixels) over two time points. 'Flower A' and 'flower B' were imaged at 'optimal' resolution (using the option and specifications provided by Zeiss LSM Browser software) at four and three time points, respectively. Every flower was observed from three angles.

Rice (*Oryza sativa* L., variety Nippon bare) crown roots were collected from young seedlings (three developed leaves) and mounted (coverslip grade 0) in a PBS buffer solution (pH 7). Imaging was carried out on an inverted Zeiss 510 META NLO multiphoton microscope in the nondescanned mode using a chameleon ultra 140 fs pulsed Ti-sapphire laser (Coherent). For cell-wall autofluorescence measurement, the laser was scanned from 690 to 770 nm range, with a peak performance at ~710 nm (which is roughly equivalent to 355 nm in single-photon excitation with a continuous wavelength laser system). Images were collected with a c-apochromat ×40, 1.2 numerical aperture (NA) (Korr uv-vis-ir) water-immersion objective.

Scalability of the MARS pipeline. We applied our MARS protocol to rice roots using a multiphoton microscope. We first acquired images of the root apex from multiple lateral views (**Supplementary Fig. 5a**); the first image stack was defined as the 'reference view' (**X**), one other view (**X′**) was diametrically opposite to this and two others were at either end of the orthogonal diameter (**Y** and **Y′**). We segmented either the reference view alone (which we called 'one-view') or the 3D reconstructions generated by fusing the following combinations of image stacks: **X** plus **X′** (two-opp-view); **X** plus **Y** or **Y′** (two-ort-view); **X** plus **X′** plus **Y** or **Y′** (three-view) or all four (four-view). The results were evaluated on a sample of about 800 manually segmented cells chosen in either the superficial cortical layer or the central meristematic zone (**Supplementary Note 5** and **Supplementary Video 3**).

Lineage tracking as an optimization problem. After each registration step of the ALT algorithm, we used the obtained common reference system to detect potential cell lineages. For every cell *i* of a given image in the sequence (source image), we look for daughter candidates $j_1, j_2, \ldots, j_k$ in the next image in the sequence (target image). Daughter candidates of *i* were identified based on their spatial proximity to *i* in the common reference system. Here these were defined as the cells *j* whose center of mass are at a distance less than a threshold distance, d_{max}, from the surface of *i* (the distance of a cell *j* to the surface of *i* is defined as the shortest distance between the center of *j* and any point of the surface of *i*). This defined a set of lineage hypotheses at this step (note that the cells belonging to the set of already determined high-confidence lineages are not taken into consideration here).

To solve the lineage problem, we then formalized the search for a set of consistent lineages between the source and target images as a combinatorial optimization problem. Here we define a valid mapping between the two images as a list of pairs of cells (*i*,*j*), *i* in the source image *I* and *j* in the target image *J* such that *j* is one of the candidate cells for cell *i*, and such that *j* appears only in one pair of the mapping (a cell of the target image cannot be a descendant of several cells in the source image). If a parent cell does not appear in a valid mapping *M*, it has no descendant in the target image by *M*. The set of such cells and the set of daughter cells that have no parent in the source image are denoted

$$\bar{I}_M \text{ and } \bar{J}_M,$$

respectively. We then attach a cost γ_{ij} corresponding to the normalized distance between *i* and *j*. We also define constant costs, γ_I and γ_J that a cell *i* has no daughters, and a cell *j* has no parent, respectively (**Supplementary Note 4**). Then, the cost of a valid mapping *M* between the source and the target image can be defined as the sum of the local cost of the pairs of cells in *M*:

$$\Gamma(M) = \sum_M \gamma_{ij} + \sum_{\bar{I}_M} \gamma_I + \sum_{\bar{J}_M} \gamma_J$$

The search for a valid lineage between the two images can then be formulated as an optimization problem: among all the possible valid mappings, we look for a single M^* with minimal cost, that is, that globally minimizes the distance between the mapped cells:

$$M^* = \underset{M \text{ valid}}{\arg\min}\, \Gamma(M)$$

To solve this optimization problem, we modeled it as a problem of flow (**Fig. 2j** and **Supplementary Note 3**), which was shown to be tractable in polynomial time[27,28].

Assessing the effect of tissue deformation between consecutive acquisitions in ALT. The ALT pipeline accuracy is critically related to the amount of change in the tissue (deformation and/or cell divisions), rather than to the time intervals between acquisitions. We tested this using serial time points where the deformation was limited (less than twofold), such as for 'plant A' at T_0, T_1 and T_2, and performed a direct tracking of cell lineages between T_0 (considered as the source image) and T_2 (as the target image), as if the image at T_1 did not exist. We found that the tracking results were markedly better between T_0–T_1 (100%) and T_1–T_2 (94%), than between T_0–T_2 (87%), hence showing that keeping time intervals short in order to limit deformation increases ALT

© 2010 Nature America, Inc. All rights reserved.

doi:10.1038/nmeth.1472

accuracy. In addition, this also decreases the required manual annotation (for example, T_0–T_1 is 100% accurate regardless of whether 4 or 22 reference lineages are provided). However, systematically decreasing time intervals from 24 h to 12 h may not be necessary as different growth transitions require different time intervals (**Fig. 3** and **Supplementary Fig. 7**).

Software. The MARS-ALT software pipeline is available as **Supplementary Software** and at http://openalea.gforge.inria.fr/dokuwiki/doku.php?id=packages:packages/. Software details are described in **Supplementary Note 5**. Time estimates for the different phases of the MARS-ALT pipeline are given in **Supplementary Table 1**.

26. Das, P. *et al.* Floral stem cell termination involves the direct regulation of *AGAMOUS* by PERIANTHIA. *Development* **136**, 1605–1611 (2009).
27. Edmonds, J. & Karp, R.M. Theoretical improvements in algorithmic efficiency for network flow problems. *J. Association Computing Machinery* **19**, 248–264 (1972).
28. Tarjan, R. *Data structures and Network Algorithms*. (Society for Industrial and Applied Mathematics, 1983).

© 2010 Nature America, Inc. All rights reserved.